PAPER

Low temperature plasma as a means to transform nanoparticle atomic structure

To cite this article: N B Uner and E Thimsen 2018 Plasma Sources Sci. Technol. 27 074005

View the article online for updates and enhancements.



IOP ebooks™

Bringing you innovative digital publishing with leading voices to create your essential collection of books in STEM research.

Start exploring the collection - download the first chapter of every title for free.

Plasma Sources Sci. Technol. 27 (2018) 074005 (13pp)

https://doi.org/10.1088/1361-6595/aad36e

Low temperature plasma as a means to transform nanoparticle atomic structure

N B Uner¹ and E Thimsen^{1,2}

- Department of Energy, Environmental and Chemical Engineering, Washington University in Saint Louis, Saint Louis, MO 63130, United States of America
- ² Institute for Material Science and Engineering, Washington University in Saint Louis, Saint Louis, MO 63130, United States of America

E-mail: elijah.thimsen@wustl.edu

Received 8 May 2018, revised 3 July 2018 Accepted for publication 13 July 2018 Published 30 July 2018



Abstract

Low temperature plasma (LTP) is a highly nonequilibrium substance capable of increasing the specific free energy of mass that flows through it. Despite this attractive feature, there are few examples of the transformation of solid material with an equilibrium atomic structure into a material with a nonequilibrium atomic structure. As a proposed example of such a transformation, in this work, it is argued that the transformation of crystalline metal nanoparticles into amorphous metal nanoparticles is feasible using LTP. To inform the feasibility calculations, detailed characterization was performed to determine the electron temperature, ion density, and background gas temperature as a function of axial position in a typical flow-through, radiofrequency, capacitively-coupled plasma reactor. Measurements revealed the existence of an intense zone with sharply elevated ion density and gas temperature in the vicinity of the powered electrode. The high intensity zone, amidst an otherwise low-intensity plasma, provides a means by which to transform the atomic structure of nanoparticles while maintaining unipolar negative charge to suppress coagulation. Theory suggests that such an intense zone would provide intense heating of nanoparticles, and subsequent rapid cooling. Calculations for copper-zirconium (CuZr) alloy show that the temperature history of a nanoparticle depends primarily on the intensity of the zone in the vicinity of the powered electrode, and on particle size. If one considers melting CuZr nanoparticles in the intense zone and then rapidly cooling them in the low-intensity plasma downstream, then the quenching rates are found to be high, on the order of 10⁵ K s⁻¹. Since quenching rates of this magnitude are sufficient to arrest an amorphous atomic structure, LTP reactors can be used to transform crystalline metal nanoparticles into amorphous metal nanoparticles via a highly nonequilibrium quenching process.

Supplementary material for this article is available online

Keywords: amorphous metal, metallic glass, low temperature plasma, nonequilibrium material

Introduction

Low temperature plasma (LTP) is increasingly being used for synthesizing and processing novel nanomaterials. As demonstrated in the last decade, by choosing appropriate precursors, many different types of nanoparticles (NP) can be synthesized, for example: group IV semiconductors [1–3], III–V semiconductors [4], metal-oxides [5], metal-sulfides [6], and pure metals [7, 8]. The unique aspect of LTP synthesis is that NPs can be made to be free standing,

unagglomerated, with a monodisperse size distribution. A key feature that enables these desirable material properties is claimed to be the unipolar charge distribution carried by particles immersed in LTP [9]. Electrostatic repulsion prevents agglomeration and coalescence, which are otherwise thermodynamically favorable processes. Another important feature of LTP is that particles have been found to have higher temperature than the surrounding gas due to ion–electron recombination at their surfaces. Direct measurements of the temperature of micron-sized particles in radiofrequency Ar

plasmas have been made using GEC reference cells [10-12]. At pressures between 0.1 and 0.4 Torr, measurements demonstrated that particle temperatures in the plasma can be approximately 100 K higher than the background gas temperature. However, in LTP synthesis of nanomaterials, higher pressures are typically employed (>1 Torr). At these higher pressures, the ion mean free path λ_i can become smaller than 10 $\lambda_{\rm D}$, where $\lambda_{\rm D}$ is the Debye radius. Thus, at higher pressures, orbital motion limited (OML) particle charging theory, which was used to model the low-pressure experiments, is expected to be inadequate to calculate ion fluxes and particle potential. The expectation is that at higher pressures in the collisional regime, where most synthesis reactors operate, NPs will have a smaller electrostatic potential but will receive an increased ion flux [13, 14]. Since the heat flux to a particle is driven by ion recombination at the surface, OML is expected to significantly underestimate the particle temperature in the plasma in the collisional regime [15].

Since the NPs in LTP synthesis reactors are usually rather small, 2-200 nm in size, direct temperature measurements are rather difficult. Evidence for intense heating of NPs has commonly been provided by indirect means, and arguments are usually supplemented by calculations. Calculations suggest that for NPs of a few nm in diameter, temperatures can reach as high as 1000 K above the background gas temperature due to their low heat capacity [16]. At such small sizes, stochastic ion-electron bombardment can lead to heat spikes, thereby elevating the particle temperature significantly above the mean particle temperature. Such stochastic heating models have been used to explain the dependence of the crystallization of Si NPs on input power to the plasma. As more power is coupled to the plasma, increasing ion fluxes can raise the NP temperature to above the crystallization temperature [17]. Similarly, the effect of ion density on the desorption of hydrogen from Si NPs has been used to estimate particle temperature by FTIR spectroscopy [18]. In another experiment, pre-synthesized metallic Bi aerosols having particle diameters in the range from 5 to 500 nm were sent into an Ar LTP [19]. It was found that the LTP vaporized the aerosol particles, even though the background gas temperature was low. Furthermore, in a recent report, the blackbody radiation emitted by 10 nm carbon NPs inside the plasma was monitored, and results suggest that particles may have reached temperatures as high as 2000 K [20].

The aforementioned highly nonequilibrium aspects of the LTP can be utilized to synthesize nanomaterials with properties that are far from equilibrium. In the context of solids, a material is in nonequilibrium state whenever it has a free energy that is higher than that of the same mass in its equilibrium state at given temperature and pressure [21]. Nonequilibrium nanomaterials can have compositions, atomic structures or size distributions that are difficult to obtain in an environment wherein local thermal equilibrium applies. Such nanomaterials can be synthesized in LTP from gaseous chemical precursors, or alternatively, premade NPs can be transformed in-flight. As an example, it was shown recently that silicon NPs can be hyperdoped with B or P during plasma synthesis to atomic concentrations that were reported to be

more than an order of magnitude higher than the solubility limit [22]. For another example, recently it was demonstrated that LTP can transform the NP size distribution to make it more monodisperse at low background gas temperature [19]. A polydisperse Bi aerosol was fed into an Ar plasma, and it was shown that the LTP focused the size distribution into a narrow range with high mass yield. Such a transformation constitutes an unexpected decrease in specific entropy, which is allowed because work is flowing into the system and heat is flowing out. Moving forward, an interesting prospect is the use of LTPs to produce materials that have a nonequilibrium atomic structure.

A clear synthetic goal for a material with a nonequilibrium atomic structure is amorphous metal NPs. At solid state, metals are typically crystalline, and thus amorphous metals have a nonequilibrium atomic structure. Amorphous metals, or amorphous metal alloys, require a synthesis route that involves a rapid quenching step that starts from either a vapor or a liquid melt. The amorphous state is imagined as a highly viscous, super-cooled liquid. The difference in free energy, between the super-cooled liquid and the crystalline equilibrium state, increases with decreasing temperature below the melting point. Quenching allows the amorphous state to be arrested and re-crystallization is extremely slow at low temperatures due to very low self-diffusion coefficients in the material. In other words, the strong thermodynamic driving force for crystallization is counteracted by slow crystallization kinetics at low temperature. Depending on the composition of the starting material, quenching rates between 10⁴ and 10⁷ K s⁻¹ are usually required to obtain amorphous binary alloys [23]. Amorphous metal NPs have unique material properties and can be used as magnets with low coercivity [24], as metal gates with uniform work function [25, 26], and as highly active catalysts [27].

In this work, we demonstrate that it is theoretically feasible to transform crystalline metal NPs into amorphous metal NPs using a modeling approach coupled with plasma characterization. The specific mechanism explored here involves using the axial ion density profile, present in typical capacitively-coupled tubular LTP reactors, to achieve a desired temperature history of NPs that flow through, which would lead to melting and subsequent rapid quenching. Measurements were conducted to obtain the profile of ion density, electron temperature, and background gas temperature along the axis of the reactor. The reactor had a flow-through configuration [28], which stands out since it offers relatively uniform particle residence times, high production rates, and continuous operation. A double Langmuir probe was used to measure ion density and electron temperature; and background gas temperature was measured by fiber optic thermometry. Measurements revealed that the plasma density exhibits a large peak in the cylindrical zone surrounded by the powered electrode, with a lower density plasma present both upstream and downstream of that zone. Similarly, compared to the low-density plasma upstream and downstream, elevated gas temperatures were measured in the vicinity of the powered electrode. Calculations performed using a particle heating model demonstrate that NPs are very rapidly heated as they enter the intense zone, and then are rapidly cooled as they exit the intense

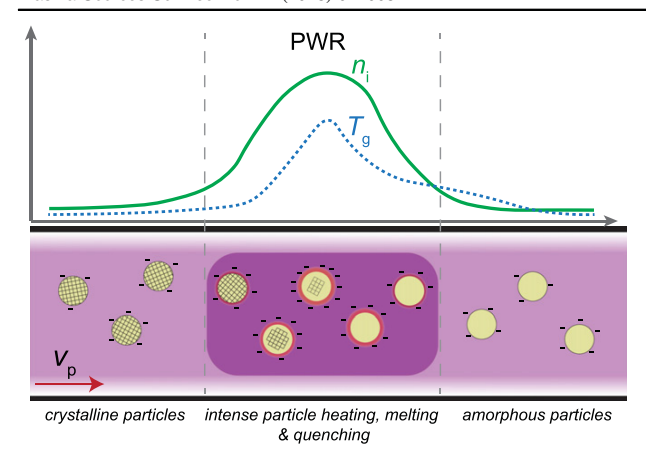


Figure 1. Schematic of the hypothesis. The nanoparticles are melted in the intense zone, which has elevated ion density and gas temperature in the vicinity of the powered (PWR) electrode, and then rapidly quenched to arrest the amorphous state in the low-intensity plasma downstream; all while maintaining a unipolar negative charge.

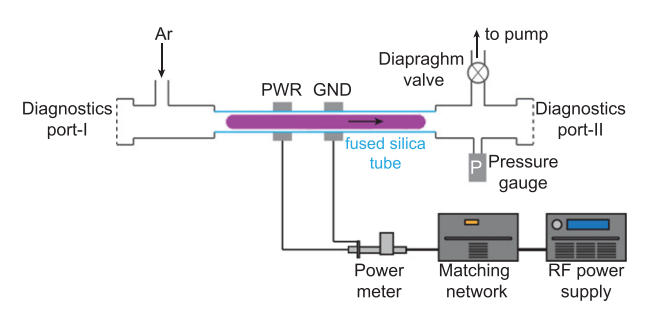


Figure 2. Experimental setup. PWR denotes the powered electrode and GND denotes the ground electrode.

zone. Importantly, since there is a low-density plasma present both upstream and downstream of the intense zone, the particles maintain a unipolar negative charge throughout the entire process, and thus, coagulation can be suppressed. As a specific example of a processing scenario for an amorphous metal, simulations were carried out for copper–zirconium (CuZr) alloy particles. CuZr is a well-established marginal glass former [29], a proven catalyst for various isomerization and hydrogenation reactions [30, 31], and a candidate for low-temperature electrocatalysis. Model calculations demonstrate that the quenching rates for NPs depends on size, but can easily exceed $10^5~{\rm K~s^{-1}}$, which is an order of magnitude higher than the experimentally measured cooling rates required to prepare amorphous CuZr by melt quenching [32]. A schematic of the key idea explored in this paper is presented in figure 1.

Methods

Experimental

This work focuses on the archetypal [28] capacitive, radiofrequency (RF) flow-through reactor that consists of a fused silica tube with an outer diameter of 1.9 cm (figure 2). Two aluminum alloy rings were placed around the tube that serve as electrodes, and an Ar plasma was generated by coupling 13.56 MHz RF power to them through an impedance matching network. The power that was transmitted from the power supply (AG0613, T&C Power Conversion, Rochester NY) through the matching network (AIT600, T&C Power Conversion, Rochester, NY) was measured with a power meter (VI Probe, Bird, Solon OH). Unless otherwise stated, all power values reported in the text are the set point values on the power supply. In addition to the ground electrode, metal parts both upstream and downstream of the silica tube were grounded. Two diagnostic ports at the ends of the reactor allowed insertion of probes into the plasma. Gas flow rate was maintained at 150 standard cubic centimeters per minute using a mass flow controller (1179C, MKS Instruments, Andover MA) and pressure was varied between 1.5 and 10 Torr with help of a diaphragm valve. A drawing of the reactor with detailed dimensions is given in the supplementary material (available online at stacks.iop.org/PSST/27/ 074005/mmedia).

The plasma parameters, electron temperature $k_{\rm B}T_{\rm e}$ and ion density $n_{\rm i}$, were measured using an RF-compensated double Langmuir probe (Impedans LTD, Dublin, Ireland). The cylindrical axis of the probe was positioned on the centerline of the glass tube. Platinum tips of 5 mm length and 0.18 mm diameter were used. Electron temperatures and ion densities were extracted from IV curves as reported in the literature [33], by assuming that the plasma was Maxwellian (see supplementary material for a sample I-V curve). The diagnostic port-I (figure 2) was only used for measurements performed at axial positions upstream of the powered electrode, and similarly, port-II was only used for measurements performed at axial positions downstream of the powered electrode.

The reactor wall temperature was measured by infrared thermometry. Thermal images were acquired using an infrared camera (SEEK Thermal Compact LW-AAA, Santa Barbara, CA) with a spectral range of $7.5-14 \,\mu\text{m}$. In this wavelength range, the fused silica tube is opaque [34], therefore the wall temperature of the reactor can be measured. The camera was calibrated for measurements conducted on the tube and on the electrodes (see supplementary material).

Background gas temperature measurements were performed by fiber optic thermometry. Electronically-conductive probes, such as thermocouples and resistance temperature detectors, are susceptible to electromagnetic interference when inserted into plasmas [35]. As an alternative, one can use the temperature-dependent florescence decay of a fluor-ophore crystal as a fundamentally different measurement principle that does not require any electronic conductors to be immersed in the plasma [36, 37]. We used two different commercially-available fluorescence decay probes (FDP), which were calibrated for different temperature ranges: 288–673 K and 423–1173 K (OptoTemp 2000, Micromaterials Inc., Tampa FL). Both probes were comprised of a composite structure of nested cylinders, which consisted of an outer alumina sheath (3.1 mm OD, 0.7 mm wall thickness)

and an inner alumina sheath (0.9 mm OD, wall thickness of 0.2 mm). The inner alumina sheath surrounded an optical fiber at the core, which was connected to the fluorophore at the tip. The tip of the high temperature probe only had the inner sheath. Images of the probes will be presented below.

It will be shown that the temperature difference between the gas and the FDP probe at the powers and pressures investigated in this study is relatively small, thus the probe temperature is a good approximation of the background gas temperature. Like any surface in contact with the plasma, it can be argued that the FDP gets hotter than the surrounding gas due to ion-electron bombardment. The reading of the FDP was corrected by an appropriate heat transfer model to ascertain the background gas temperature. The charging regime that applies to the probe is distinguished by 4 characteristic lengths: the electron mean free path (λ_e) , radius of the zone containing the layer of positive space charge (R_0) , probe radius (r_{pr}) and ion mean free path (λ_i) . The electron mean free path, λ_e is expected to be similar to or greater than R_0 , and R_0 is similar in magnitude to $r_{\rm pr}$, since $\lambda_{\rm D} + r_{\rm pr} \approx R_0$ and $\lambda_{\rm D} \ll r_{\rm pr}$ [38]. We use $\lambda_{\rm D} \approx \lambda_{\rm Di} = (\varepsilon_0 k_{\rm B} T_{\rm i}/e^2 n_{\rm i})^{1/2}$, where ε_0 is the permittivity of vacuum, e is unit charge, $k_{\rm B}$ is the Boltzmann constant and T_i is ion temperature. Thus, the hierarchy of the characteristic lengths is as follows: $\lambda_e \gtrsim R_0$, $R_0 \approx r_{
m pr}$, and $r_{
m pr} \gg \lambda_{
m i}$. Under such conditions, the ion and electron fluxes to the tip of the probe can be described by the following equations [38, 39]:

$$J_{\rm i} = \frac{\pi}{8} n_{\rm i} \beta_{\rm i} \frac{\lambda_{\rm i}}{r_{\rm pr}} \left(1 + \frac{T_{\rm e}}{T_{\rm i}} \right),\tag{1}$$

$$J_{\rm e} = \frac{1}{4} n_{\rm e} \beta_{\rm e} \exp\left(\frac{e\phi}{k_{\rm B} T_{\rm e}}\right). \tag{2}$$

In equations (1) and (2), subscripts 'i' and 'e' denote ion and electron respectively. J is the flux, n is the number density, $T_{\rm e}$ is electron temperature, ϕ is probe potential and β is the mean thermal velocity. For ions and electrons, β is defined as $(8k_{\rm B}T_{\rm i,e}/\pi m_{\rm i,e})^{1/2}$, where $m_{\rm i}$ and $m_{\rm e}$ are the masses of Ar ions and electrons respectively. Since the probe is not conductive, the net current flowing onto the probe is zero. Therefore, flux matching can be used to determine the probe potential:

$$J_i = J_e. (3)$$

The probe potential and the corresponding ion fluxes enter into the energy balance of the probe, which at steady-state is:

$$q_{\rm ie} = q_{\rm conv} + q_{\rm rad} + q_{\rm cond},\tag{4}$$

where $q_{\rm ie}$ denotes the heat flux onto the probe due the ion and electron bombardment. The probe absorbs heat from ion–electron recombination on the surface, and from the transfer of kinetic energy of bombarding electrons and ions that are accelerated in the sheath. Hence, the heat flux to the probe due to ion and electron bombardment can be given as:

$$q_{\rm ie} = J_{\rm i}(|\Delta H_{\rm rec}| + {\rm KE}) = J_{\rm i}(|\Delta H_{\rm rec}| + e|\phi| + 2k_{\rm B}T_{\rm e}),$$
 (5)

where $|\Delta H_{\rm rec}|$ is the recombination energy (15.76 eV for Ar). The terms $e|\phi|$ and $2k_{\rm B}T_{\rm e}$ account for the conversion of

kinetic energy, from ions and electrons respectively, into internal energy in the probe. On the right-hand side of equation (4), fluxes representing heat loss due to convection, radiation exchange with the walls and conduction are given. The conduction term is omitted in this work. The convection and radiation terms can be expressed as:

$$q_{\rm conv} = h(T_{\rm pr} - T_{\rm g}), \tag{6}$$

$$q_{\rm rad} = \varepsilon \sigma_{\rm SB} (T_{\rm pr}^4 - T_{\rm w}^4), \tag{7}$$

where h is the convective heat transfer coefficient, $T_{\rm pr}$ is the probe temperature, $T_{\rm g}$ is the gas temperature, $T_{\rm w}$ is the wall temperature, ε is the emissivity of the alumina probe surface and $\sigma_{\rm SB}$ is the Stefan–Boltzmann constant. The view factor corresponding to the probe tip and the reactor walls is neglected in equation (7), which leads to a slight underestimate of radiative cooling in the zone surrounded by the powered electrode.

Numerical solutions of equations (3) and (4) were used to correct the probe measurement to determine the background gas temperature (see supplementary material). Both the raw measurement of the probe and the corrected values, termed the background gas temperature, are reported (*vide infra*).

As an aside, if one wishes to make a short-cut estimate of the expected difference between gas and probe temperature ΔT , the kinetic energy contribution to equation (5) can be obtained by solving for the probe potential in equations (1)–(3):

$$KE = \left\{ \left| \ln \left[\frac{\pi}{2} \sqrt{\frac{T_i m_e}{T_e m_i}} \left(\frac{\lambda_i}{r_{pr}} \right) \left(1 + \frac{T_e}{T_i} \right) \right] \right| + 2 \right\} k_B T_e. \quad (8)$$

The contribution of heat input to the probe due to kinetic energy transfer is expected to be 15–30 eV, depending on $r_{\rm pr}$, $\lambda_{\rm i}$, $T_{\rm e}$ and $T_{\rm i}$. Throughout this paper, it is assumed that the ion temperature is the same as the background gas temperature. By substituting the maximum value predicted by equation (8) into (5), equations (4), (6) and (7) yield the maximum difference between gas and probe temperature:

$$\Delta T \approx \frac{3J_{\rm i}|\Delta H_{\rm rec}| - \varepsilon \sigma_{\rm SB}(T_{\rm pr}^{\ 4} - T_{\rm w}^{\ 4})}{h},\tag{9}$$

where $J_{\rm i}$ is to be calculated from equation (1). For the low and high temperature probe, conservative estimates for the heat transfer coefficient are found to be 35 and $72\,{\rm W\,m^{-2}\,K^{-1}}$ respectively [40], which are independent of pressure (see supplementary material for details). By using measured values of $n_{\rm i}$, $T_{\rm e}$ and $T_{\rm w}$, ΔT can be calculated to check whether probe temperature is representative of the gas temperature.

Numerical model

In the numerical model, an aerosol-based process is considered, wherein crystalline CuZr NPs are fed into the reactor, similar to the study given in [19]. The temperature history of the CuZr NPs is calculated by using the experimentally measured profiles of electron temperature, ion density, and background gas temperature as inputs. We consider spherical particles that have

a diameter of 20 nm or larger. These particles were assumed to have a monodisperse size distribution with sufficiently low particle concentrations ($\pi n_{\rm p} d_{\rm p}^2 < 0.01~{\rm m}^{-1}$, where $n_{\rm p}$ and and $d_{\rm p}$ are total particle number concentration and particle diameter respectively), such that $n_{\rm i} = n_{\rm e}$ and the electron temperature of the pristine plasma is unperturbed. The model solves for: (1) charge distribution, (2) particle temperature, and (3) particle velocity.

Nanoparticle charge distribution. As NPs enter the plasma they quickly become charged and a charge distribution develops. A single-step Markov process describes the charge distribution on a monodisperse aerosol [41]:

$$\frac{1}{\pi d_{p}^{2}} \frac{dF_{Z}}{dt} = (J_{i} + J_{TE})_{Z-1} F_{Z-1} - (J_{i} + J_{e}) + J_{TE})_{Z} F_{Z} + (J_{e})_{Z+1} F_{Z+1},$$
(10)

where F_Z is the fraction of particles having charge Z, t is residence time, $d_{\rm p}$ is the particle diameter, and $J_{\rm TE}$ is the electron flux due to thermionic emission. Subscript Z used with the brackets stand for the charge that the fluxes are evaluated with. For NPs, the charging regime is different than that of the FDP. First of all, particle charging regime is slightly collisional since $\lambda_{\rm i} < 10~\lambda_{\rm D}$ [14]. Hence, the ion flux can be given by the following equation:

$$J_{\rm i} = \left[\frac{1}{J_{\rm i,CEM}} + \frac{1}{J_{\rm i,HYD}} \right]^{-1}.$$
 (11)

 $J_{i,CEM}$ represents the ion flux in the collision enhanced mechanism of ion collection [13, 14]:

$$J_{i,\text{CEM}} = \frac{1}{4} n_i \beta_i \left[1 - \frac{e\phi_p}{k_B T_i} + 0.1 \left(\frac{e\phi_p}{k_B T_i} \right)^2 \left(\frac{\lambda_D}{\lambda_i} \right) \right]. \tag{12}$$

 $\phi_{\rm p}$ is the shielded particle potential:

$$\phi_{\rm p} = \frac{eZ}{2\pi\varepsilon_0 d_{\rm p}} e^{-d_{\rm p}/2\lambda_{\rm D}}.$$
 (13)

The first two terms inside the square brackets of equation (12) arise from OML theory. The third term is an approximate correction factor for single collisions between ions and neutrals in the sheath of the NP. Equation (12) is suitable for the cases where $\lambda_i > d_p$. In equation (11), $J_{i,HYD}$ accounts for the ion flux described by the hydrodynamic mechanism in the continuum regime, which dominates the ion flux in the case when the sheath is highly collisional [39]:

$$J_{i,HYD} = \sqrt{\frac{\pi}{2}} n_i \beta_i \left(\frac{\lambda_i}{d_p} \right) \left| \frac{e \phi_p}{k_B T_i} \right|. \tag{14}$$

Equation (14) is valid when $\lambda_i < d_p$, which is the opposite side of the regime that equation (12) is used for. The bracket of equation (11) is the interpolation formula presented in [42] that bridges different charging regimes, and it has a common mathematical form that is used to cover transport phenomena occurring on free molecular, transition and continuum regimes [43]. λ_i is the parameter defining the collisionality. As pressure increases, λ_i decreases, thus equation (12)

overpredicts fluxes when the pressure is high. A similar overprediction in ion fluxes is obtained from equation (14) when the pressure is too low. Therefore, equation (11) allows the determination of the appropriate ion flux expression at a given pressure. With all charging terms included, equation (11) is termed the collisional model (CM). If the model is described as OML, then only the OML terms are considered (i.e. $J_{i,HYD}$ is ignored and the third term inside the square brackets of equation (12) is ignored). Since λ_e is large, we use the expression given by equation (2) for J_e in equation (10).

The thermionic flux is given by the Richardson-Dushman equation:

$$J_{\text{TE}} = bA_0 T_p^2 \exp\left(-\frac{W}{k_{\text{B}} T_p}\right),\tag{15}$$

where $T_{\rm p}$ is the particle temperature, W is the work function for the particle, A_0 is the Richardson–Dushman constant (= $1.202 \times 10^6 \, {\rm A \, m^{-2} \, K^{-2}}$) and b is a material dependent correction factor. The lowering of work function due to the field on the surface of a negatively charged particle is incorporated via the Schottky expression:

$$W = W_0 - \frac{e^2|Z|}{2\pi\varepsilon_0 d_p} \tag{16}$$

 W_0 is the work function of the bulk material.

The charging process is rapid when compared to other processes that a particle experiences within the plasma. In supplementary material, the time required for a particle to obtain the mean charge was derived as:

$$\tau_{\rm C} = \left[\frac{1}{\tau_{\rm OML}} + \frac{1}{\tau_{\rm CEM}}\right]^{-1}.\tag{17}$$

The term $au_{\rm OML}$ describes the charging time for the OML theory and $au_{\rm CEM}$ is the contribution due to the collision enhanced mechanism:

$$\tau_{\text{OML}} = \frac{8\lambda_{\text{D}}^2}{\beta_{\text{i}}d_{\text{p}}},\tag{18}$$

$$\tau_{\text{CEM}} = 40 \frac{\lambda_{\text{i}} \lambda_{\text{D}}}{\beta_{\text{i}} d_{\text{p}}} \left(\frac{e |\phi_{\text{p}}|}{k_{\text{B}} T_{\text{i}}} \right)^{-1}.$$
 (19)

The time $\tau_{\rm C}$ can be compared to the time required for a particle to move a distance over which a significant change in ion density occurs. Let $x_{\rm m}$ be the axial distance over which there is a change in ion density, which is approximately 1 mm (vide infra). When $x_{\rm m}$ is divided by the gas velocity (vide infra), an estimate can be made for the time it takes the ion density to change, $\tau_{\rm R} = x_{\rm m}/v_{\rm g}$, which is less than or equal to $100~\mu s$. The charging times for the cases investigated in this study are few μs , as determined from equation (17). Since the charging time is much smaller than the time during which a particle experiences a difference in the surrounding ion density, the solution to equation (10) can be simplified by assuming steady-state [41]. From the steady-state charge distribution, the average charge and the standard deviation were calculated. At the pressures investigated, the

hydrodynamic charging term has a minor effect on the particle charge. Furthermore, the effect of the thermionic emission on the particle charge is negligible at temperatures below 2000K (*vide infra*).

Nanoparticle heating. A monodisperse aerosol traveling through the reactor satisfies the following transient energy balance equation:

$$\frac{d(m_{\rm p}H_{\rm p})}{dx} = \pi d_{\rm p}^2 n_{\rm p} (q_{\rm ie} - q_{\rm Kn} - q_{\rm rad} - q_{\rm TE}), \qquad (20$$

where x represents the axial coordinate in the reactor, $m_{\rm p}$ is the mass flux of the aerosol and it is equal to $v_{\rm p}n_{\rm p}(\pi/6)d_{\rm p}^3\rho_{\rm p}$, $v_{\rm p}$ is the particle velocity and $\rho_{\rm p}$ is the mass density of the material comprising the nanoparticle. $H_{\rm p}=C_{\rm p}T_{\rm p}$ denotes the mass specific enthalpy of the particles with $C_{\rm p}$ being the specific heat capacity. The bracket on the right-hand side of equation (20) contains fluxes for plasma heating and cooling due to conduction, radiation and thermionic emission. Evaporation was omitted, since the vapor pressure of the CuZr alloy is expected to be low at most of the particle temperatures that were investigated. Equation (20) can be rearranged as:

$$\frac{dT_{\rm p}}{dx} = \frac{1}{v_{\rm p}} \left[\frac{6}{\rho_{\rm p} C_{\rm p} d_{\rm p}} (q_{\rm ie} - q_{\rm Kn} - q_{\rm rad} - q_{\rm TE}) - T_{\rm p} \frac{dv_{\rm p}}{dx} \right]. \tag{21}$$

This equation is one of the main equations that we solve, along with the steady-state form of equation (10). The second term in the brackets incorporates the effect of particle acceleration on particle temperature ($vide\ infra$). The heating term q_{ie} has slight modifications when compared to the analog used for the FDP:

$$q_{\rm ie} = J_{\rm i}(|\Delta H_{\rm rec}| - W + fe|\phi_{\rm p}|) + 2J_{\rm e}k_{\rm B}T_{\rm e}.$$
 (22)

The heat input is reduced by the work function of the particle (equation (16)) and a fraction of the kinetic energy of the bombarding ions, given as f, is absorbed. The contributions from the energy exchange with metastable species and the absorption of plasma radiation were neglected since they have been argued to be insignificant when compared to $q_{\rm ie}$ [44]. The charge distribution leads to particles with different potentials. Since a change in particle potential results in different electron and ion fluxes to the particle surface, a temperature distribution develops across the monodisperse aerosol. All particles cool down due to heat exchange with the surrounding gas. Since the Knudsen number, $\mathrm{Kn} = 2\lambda_{\mathrm{g}}/d_{\mathrm{p}}$ with λ_{g} being the mean free path of neutral gas atoms, is larger than 10 [45], we use the Knudsen expression for heat transfer in the free molecular regime [46]:

$$q_{\rm Kn} = \frac{1}{2} \alpha_{\rm H} \beta_{\rm g} \frac{P}{T_{\rm g}} (T_{\rm P} - T_{\rm g}), \qquad (23)$$

where $\alpha_{\rm H}$ is the thermal accommodation coefficient and *P* is pressure. The radiation cooling term in equation (21) is given by equation (7). Emissivity of a small particle equals to the absorption cross section due to Kirchoff's law [47], and it is a

function of temperature and size. The Rayleigh–Penndorf approximation is used to evaluate the emissivity [48] (see supplementary material for details). The cooling due to thermionic emission is given as:

$$q_{\rm TF} = J_{\rm TE}W. \tag{24}$$

For low particle temperatures, the thermionic emission terms in equations (10) and (21) are dropped out, unless otherwise noted. Without the thermionic emission terms, charging and heating are decoupled.

The use of a lumped in space and continuous in time formulation for $T_{\rm p}$ can be justified from the Biot number, which is orders of magnitude smaller than 1, and from the relatively large heat capacity of the particles. The particles are expected to thermally equilibrate at a rate depending on their size and the overall heat transfer coefficient inside the plasma. This equilibration time can be given as [10]

$$\tau_{\rm H} = \frac{d_{\rm p}\rho_{\rm p}C_{\rm p}}{6U},\tag{25}$$

where U is an approximate form of the overall heat transfer coefficient:

$$U = \sigma_{\rm SB} \varepsilon (T_{\rm p\infty}^3 + T_{\rm w}^3) + \frac{1}{2} \alpha_{\rm H} \beta_{\rm g} \frac{P}{T_{\rm g}}.$$
 (26)

 $T_{\rm p\infty}$ stands for the final particle temperature obtained at the end of the heating process. At 1.5 Torr, the equilibration time of a 20 nm particle is less than 100 μs within the particle temperatures explored, that is $\tau_{\rm H} \approx \tau_{\rm R}$. Therefore, we expect the 20 nm particle to be at a steady-state temperature inside the plasma. However, larger particles will experience a lag in heating.

At high particle temperatures, particles can melt. Melting is taken into account in a classical way, and any pre-melting phenomena and size effects are neglected. Size effects, if they were included, would cause the nanoparticles to melt at a temperature less than $T_{\rm m}$ [49], which is the melting temperature $T_{\rm m}$ of bulk CuZr (see supplementary material). At $T_{\rm p}=T_{\rm m}$, the evolution of the melt fraction y_{ℓ} can be described with the following equation:

$$\frac{dy_{\ell}}{dx} = \frac{1}{v_{p}} \left[\frac{6}{\rho_{p} L d_{p}} (q_{in} - q_{Kn} - q_{rad} - q_{TE}) - y_{\ell} \frac{dv_{p}}{dx} \right]$$
(27)

which is similar to equation (21). L is the enthalpy of melting. The \sim 3% increase in particle size upon complete melting is omitted.

Nanoparticle velocity. Since the gas flow accelerates due to the higher temperature zone in the vicinity of the powered electrode, NPs will also accelerate and adapt to the changes in gas velocity. Acceleration will cause particles to spend less time in the locations where gas temperature is elevated. In our case, the particle Reynolds numbers, $Re_p = d_p v_g \rho_g / \mu$ are much lower than 1, and thus, the Stokes regime applies. The velocity of the particle as a function of position in the reactor

is given as [45]:

$$\frac{dv_{p}}{dx} = -\frac{18\mu}{\rho_{p}d_{p}^{2}C_{c}} \left(1 - \frac{v_{g}}{v_{p}}\right),\tag{28}$$

where μ is the viscosity of Ar and C_c is the Cunningham slip correction factor:

$$C_c = 1 + \text{Kn}(1.257 + 0.4e^{-1.1\text{Kn}}).$$
 (29)

The gas velocity in equation (28) can be calculated from continuity and the ideal gas law:

$$v_{\rm g} = v_{\rm g0} \frac{T_{\rm g}}{T_{\rm o}},\tag{30}$$

where T_0 is the ambient temperature equal to 294 K. The gas mass flow rate was the set point on the flow controller and the $v_{\rm g0}$ corresponds to the average gas velocity at the inlet temperature, which was $6.8\,{\rm m\,s^{-1}}$. The material properties used in the model are tabulated in the supplementary material.

Results and discussion

Experimental

All three independent sets of diagnostics revealed an intense zone proximate to the powered electrode, within an otherwise low-intensity plasma (vide infra). At 1.5 Torr, axial scans conducted with the double Langmuir probe at power set points of 10 and 20 W showed that the electron temperature was nominally independent of axial position and power (figure 3(a)). However, there was a maximum in the ion density at the center of the zone surrounded by the powered electrode and this maximum became greater with power increasing from 10 to 20 W (figure 3(b)). In fact, the results in figure 3(b) suggest that the ion density in the low-intensity plasma did not change significantly with increasing applied power. At 20 W, the ion densities measured in the intense zone were approximately 5 times higher than the densities measured in the low-intensity plasma at positions further away. Plasma emission spectra collected at different locations showed that Ar II emission lines were detectable only near the powered electrode, providing further evidence for the existence of the intense zone (see supplementary material).

Since changing the applied power primarily affected the ion density in the zone surrounded by the powered electrode, while the low-intensity plasma remained approximately constant, further measurements focused on the plasma parameters at the peak position as a function of external process parameters. Plotted in figure 4 are the electron temperature and ion density as a function of the applied RF power for two different pressures: 1.5 and 10 Torr. At 1.5 Torr, the electron temperature increased slightly from 1.9 to 3.2 eV with applied power in the range from 10 to 60 W (figure 4(a)). Higher powers were not explored, due to extensive contamination of the double Langmuir probe, which caused the *IV* curves to become increasingly skewed, leading to an erroneous increase in the apparent electron temperature [50]. At a pressure of 10 Torr, the electron temperature was nominally independent

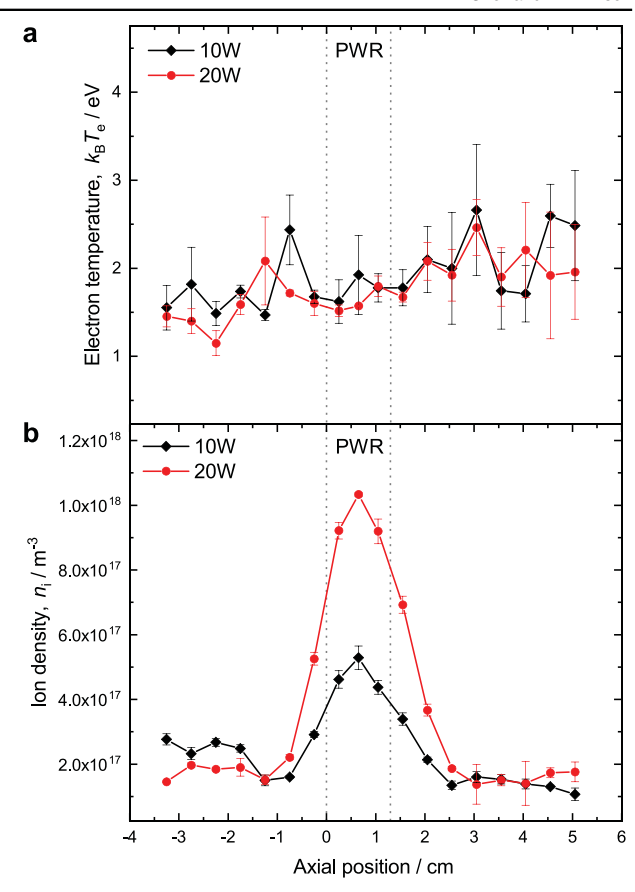


Figure 3. Axial profile of plasma parameters. (a) Electron temperature and (b) ion density along the central axis of the reactor measured at 1.5 Torr for different applied power set points.

of applied power, and slightly greater than 2 eV. At both pressures, the ion density increased with applied power in the range from 10^{17} to $10^{18} \, \text{m}^{-3}$ (figure 4(b)); and the measured ion density at 1.5 Torr was greater than at 10 Torr. A summary of the plasma parameters measured in the intense zone at 1.5 Torr as a function of applied power is given in table 1.

The temperature of the reactor wall, as measured from infrared thermal images, also obtained a maximum value in the vicinity of the powered electrode. A hot spot was observed around the powered electrode at all powers and pressures (figures 5(a) and (b)). RF power measurements revealed that the matching network transmitted approximately 2/3 of the power sent by the power supply (table 1). This power was coupled to the plasma and appeared to be dissipated primarily in the intense zone. Measurements showed that the wall temperature approached 650 K at a set power of 70 W (figure 5(c), table 1). The wall temperature is an important piece of information that is required to determine the radiative heat exchange for the FDP and the particles. In addition, since the wall temperature is clearly related to the temperature of the gas flowing through the reactor, a maximum in the background gas temperature is also expected in the vicinity of the powered electrode.

FDP measurements also revealed an intense zone in the vicinity of the powered electrode, specifically a maximum in

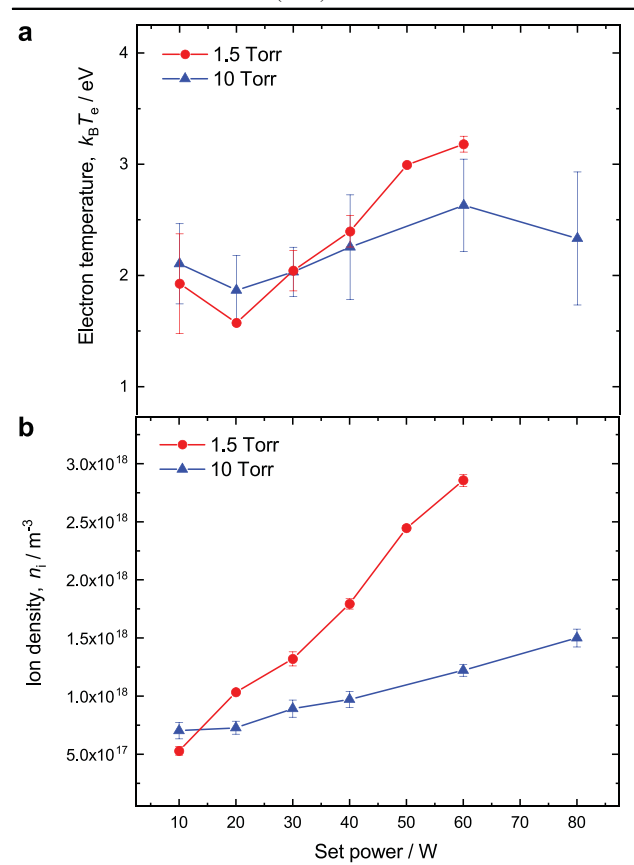


Figure 4. Plasma parameters measured at the center of the zone surrounded by the powered electrode. (a) Electron temperature and (b) ion density as a function of RF power.

the background gas temperature. A photo of the low temperature probe inserted in the zone surrounded by the powered electrode is presented in figure 6(a), and a photo of the high temperature probe outside the reactor in figure 6(b). FDP measurements were made as a function of axial position. Measurements were corrected by using the heat transfer model described in the methods section, using the experimentally determined plasma parameters and wall temperature as inputs. As discussed in the methods section when deriving equation (9), the difference between the probe temperature and the calculated gas temperature was found to be small. Probe and background gas temperatures were found to be approximately equal at 10 Torr. Both the raw and corrected values are presented in figure 6(c) as a function of axial position for 10 and 20 W of applied RF power. For 20 W, the background gas temperature peaked at approximately 420 K. Since the peak temperature was observed in the zone surrounded by the powered electrode, the effect of applied power and total gas pressure was studied only at that axial location (figure 6(d)). The probe temperature increased with applied power, apparently reaching values of nearly 1000 K at applied power set point of 80 W. In our experiments, at a given applied power, increasing the pressure from 1.5 to 10 Torr generally had the effect of lowering the background gas temperature, which can be explained by increased cooling rate and lower ion density (figure 4(b)). These results clearly emphasize the need to experimentally characterize the background gas temperature, since it appears to be well above room temperature at commonly used applied RF powers. The results for 1.5 Torr total pressure are summarized in table 1 (vide supra).

The intense zone is of paramount importance to realizing the rapid heating and cooling of NPs. The observation of an intense zone in the vicinity of the powered electrode is consistent with reports in the literature that involve similar reactors. In a study conducted on the synthesis of Si NPs in a similar flow-through reactor, NPs were sampled from the reactor at different locations [52]. It was shown that particles become crystalline only after they passed through the powered electrode. In another study, by monitoring the optical emission from the plasma, an aerosol of Bi particles was observed to vaporize only in the vicinity of the powered electrode [19]. Furthermore, computational modeling of a similar reactor found elevated ion density and gas temperature near the powered electrode [53]. Thus, the results presented below are expected to be qualitatively general to the type of LTP reactor described herein, while the quantitative details will of course depend on pressure, applied power, reactor size, and etc.

Numerical model

The question explored with the model is: can the NP temperature be made to exceed the melting point of CuZr in the intense zone, and then cool to below the crystallization temperature sufficiently fast to arrest the amorphous state? Answering this question requires the calculation of particle temperature histories in the LTP. By using the measured plasma parameters and temperatures given in the previous section, temperature histories were obtained by solving the heat and particle velocity equations (21) and (28), where equation (27) was substituted for equation (21) whenever a particle was melting. The numerical solution of these differential equations was accompanied by a steady-state solution of the charging equation (10), which utilizes equations of detailed balance [41]. Since the particle sizes that we consider were larger than 10 nm and since they were of sufficiently low concentration, the particles carried a unipolar negative charge. Figure 7 provides an example charge distribution and a steady-state temperature distribution for a monodisperse aerosol with 50 nm particles. Distributions are plotted for two different charging models: CM and OML (see methods section). OML predicts a higher particle charge and lower temperatures. On the other hand, CM leads to decreased particle charge due a higher ion flux, which eventually leads to higher temperatures. Although a slight increase in particle temperature due to CM when compared to OML has been discussed [15, 54], in our case, the discrepancy is much more dramatic. In both models, the particle temperature increases with increasing charge, and thus, the charge distribution causes a temperature distribution. The very high particle temperatures predicted by the CM model provide a means by which to melt particles in the plasma.

Table 1. Experimental data summary. Power, temperature and plasma density measurements conducted at 1.5 Torr. Plasma parameters were obtained at the center of the zone surrounded by the powered electrode. The variation in the measured plasma parameters indicates three standard deviation bounds.

$P_{\text{set}} (\mathbf{W})^{\mathbf{a}}$	$P_{\rm m} (\mathrm{W})^{\mathrm{b}}$	$T_{\rm w} ({\rm K})^{\rm c}$	$T_{\rm pr}\left({\rm K}\right)$	$k_{\rm B}T_{\rm e}~({\rm eV})$	$n_{\rm i} \times 10^{18} ({\rm m}^{-3})$
10	7	334	367	1.93 ± 1.33	0.53 ± 0.11
20	13	390	413	1.57 ± 0.02	1.03 ± 0.02
30	19	444	483	2.04 ± 0.54	1.32 ± 0.18
40	25	507	578	2.40 ± 0.52	1.79 ± 0.14
50	31	556	668	3.00 ± 0.06	2.45 ± 0.06
60	38	592	753	3.18 ± 0.21	2.86 ± 0.15
70	44	630	863	_	_
80	52	>650	963	_	_

 P_{set} is the set point on the RF power supply.

 $^{^{\}circ}$ $P_{\rm m}$ is the measured power delivered to the electrodes. All measurements had a maximum variability of ± 1 W. $P_{\rm m}$ was found to be approximately equal to 2/3 $P_{\rm set}$. $^{\circ}$ $T_{\rm w}$ is the maximum wall temperature recorded at each applied power, which occurred in the vicinity of the powered electrode.

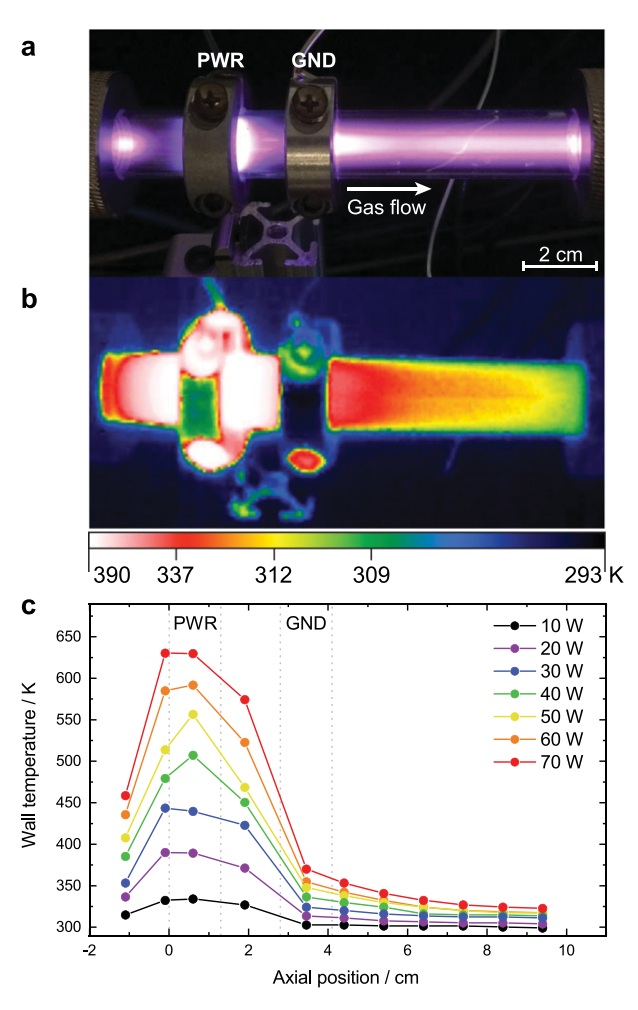


Figure 5. Reactor wall temperature. (a) Photograph of the reactor and the Ar plasma with 20 W power and at 1.5 Torr. (b) Thermal image taken at the same conditions given in (a). The scale bar represents the calibration done on glass (see supplementary material). (c) Wall temperature measurements at 1.5 Torr as a function of power and position. Figures (a) and (b) were reprinted from [51], with the permission of American Vacuum Society.

The calculated NP temperature reaches a maximum in the intense zone and then rapidly drops in the low-intensity plasma downstream. Temperature histories of 50 nm diameter particles at 1.5 Torr are given in figure 8. The temperatures of particles having the mean charge are plotted for two different applied powers, 10 and 20 W. At 10 W, the difference between the particle temperature predicted by the OML and CM is approximately 100 K in the regions sufficiently far away from the electrode. However, the difference in predicted temperatures increases to 300 K at the center of powered electrode. The discrepancy between the theories increases further to 500 K at the center of the electrode when the power is set to 20 W. The divergence in the predictions of NP temperature for CM and OML is quite sensitive to ion density. The plateau in the particle temperature history of the particle modeled with CM at 20 W is due to melting, which is an isothermal process.

Nanoparticle size plays a major role in the peak NP temperature reached in the intense zone. Smaller NPs reach a higher temperature as a result of their higher surface area to volume ratio, which allows them to respond more rapidly to changes in the plasma parameters and background gas temperature at different axial positions. Larger particles have a higher thermal inertia as a result of their lower surface area to volume ratio and take longer to heat up and cool down (equation (25)). NP temperature as a function of axial position and particle size is plotted in figure 9(a), for CuZr NPs of 20, 200 and 500 nm in diameter. As the NP diameter increases, the peak temperature decreases and the axial position at which the maximum occurs shifts to positions further downstream. The distribution in NP temperature, which is described by the shaded region in figure 9(a), corresponds to the temperature of particles having ± 1 standard deviation of the NP charge distribution. Since the measured ion densities are nearly symmetric around the electrode (figure 3(b)), the heating and cooling rates in the vicinity of the powered electrode are approximately equal. All particles carry a unipolar negative charge in both the high-intensity and low-intensity zones of the plasma. The average charge is plotted in figure 9(b),

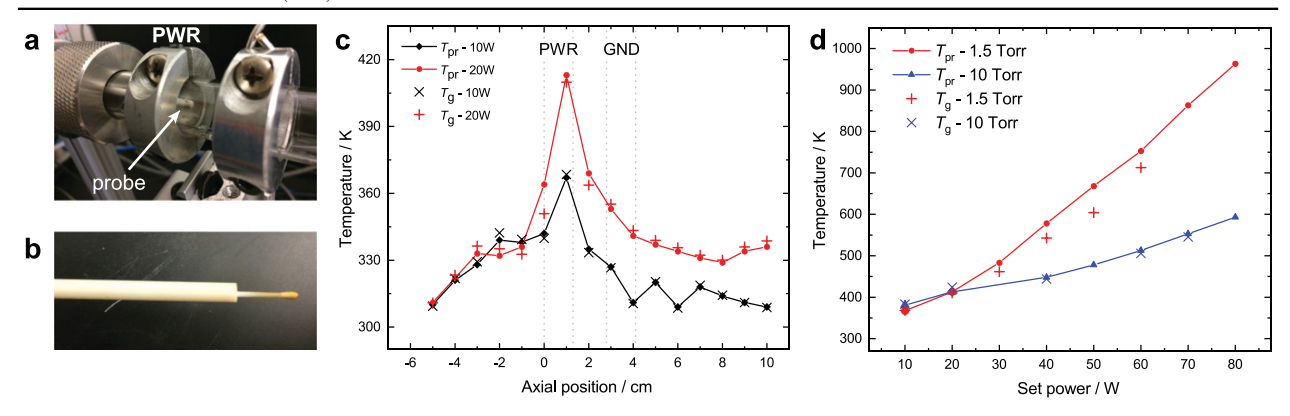


Figure 6. Background gas temperature. (a) Low temperature probe (288–673 K) inserted into the reactor. (b) High temperature probe (423–1173 K). (c) Probe temperature ($T_{\rm pr}$) and calculated gas temperatures ($T_{\rm g}$) as a function of position at 1.5 Torr. (d) Probe temperatures and calculated gas temperatures in the zone surrounded by the powered electrode as a function of power and pressure.

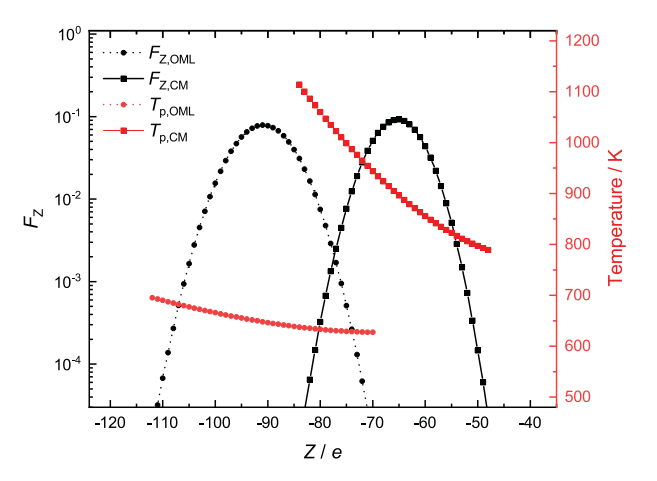


Figure 7. Particle charge and temperature distributions with different charging models. F_Z is the fraction of nanoparticles having charge Z (equation (10)). The nanoparticles were monodisperse 50 nm diameter $\text{Cu}_{58}\text{Zr}_{42}$. The following plasma parameters were used for an Ar plasma: $n_{\rm i} = 5 \times 10^{17} \, \text{m}^{-3}$, $k_{\rm B}T_{\rm e} = 2 \, \text{eV}$, $T_{\rm g} = 370 \, \text{K}$, $T_{\rm w} = 335 \, \text{K}$, $P = 1.5 \, \text{Torr}$.

where the shaded region corresponds to ± 1 standard deviation of the distribution. For smaller particles, the peak temperature in the intense zone exceeds the melting point of CuZr. However, particles start melting at different times and their melting periods are different due to the temperature distribution. Larger NPs are more difficult to heat up, and would most likely require higher powers to reach the requisite ion densities to melt the particle (figure 4(b)). Other possibilities to melt larger NPs would be having a broader intense zone, or increasing the residence time spent in the zone.

With sufficiently long residence times inside the intense zone, or with higher applied power, the maximum particle temperatures can be increased above 2000 K. Figure 10 shows the mean values of particle temperature distribution inside the intense zone obtained by solving for the steady-state conditions in equation (21). It was found that at temperatures above 2000 K, the thermionic emission terms in equations (10) and (21) can become comparable in magnitude to other charging and cooling mechanisms. Thermionic

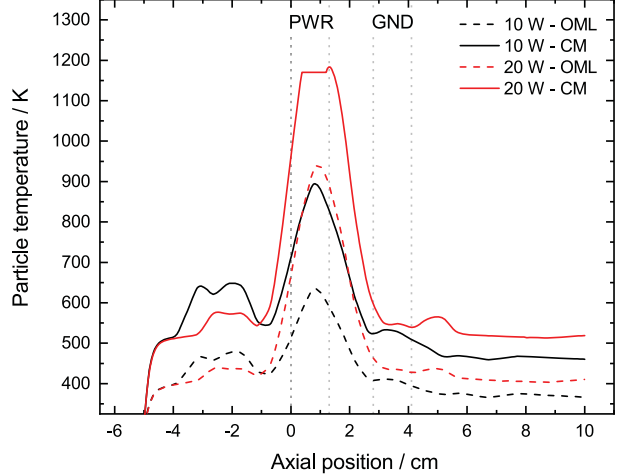


Figure 8. Nanoparticle temperature histories for different applied powers and charging models. The nanoparticles were monodisperse 50 nm diameter $\text{Cu}_{58}\text{Zr}_{42}$. Temperatures of the particles with a charge that is the average of the distribution were plotted. The red curves are for a power set point of 20 W and the black curves are for 10 W. The dashed lines are for charging described by only OML and the solid lines for charging described by CM.

emission shifts the particle charge distribution to a lower mean charge, and this shift is accompanied by decreased heat influx onto the particle. Accordingly, thermionic emission terms were retained in these steady-state calculations. For the 20 nm particle, which is already at steady-state as it travels through the intense zone, particle temperatures can reach 2000 K at 1.5 Torr for powers above 40 W. At temperatures greater than 2000 K, thermionic emission is seen to limit the particle temperature. We expect evaporation to be an important cooling mechanism at such temperatures as well. At steady-state, the 200 nm particle is seen to reach a temperature that is higher than its melting point at 20 W, which is about 150 K higher than the maximum value given in figure 9(a). We estimate that the width of the intense zone should be a centimeter broader than its original width (1.3 cm) for a 200 nm particle to melt at 20 W. It was observed that thermionic emission does not limit the temperature of the

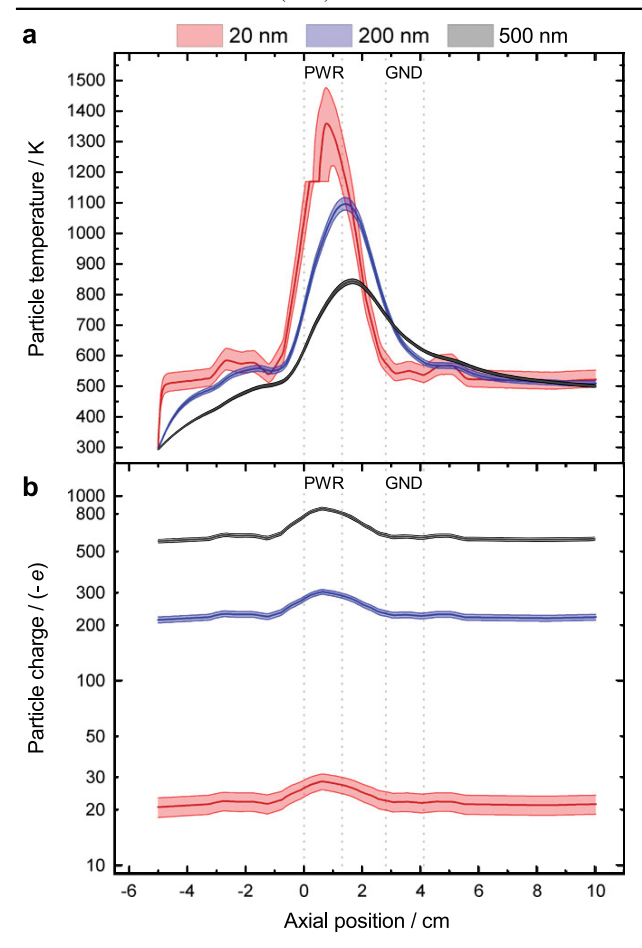


Figure 9. Effect of particle size on temperature history. (a) Temperature histories of $Cu_{58}Zr_{42}$ particles of different sizes as a function of axial position, predicted by the CM charging model at an applied power set point of 20 W and a total pressure of 1.5 Torr. The bands correspond to the distribution in nanoparticle temperatures due to the charge distribution. (b) Evolution of particle charge for particles simulated in (a). The bands correspond to the ± 1 standard deviation limits.

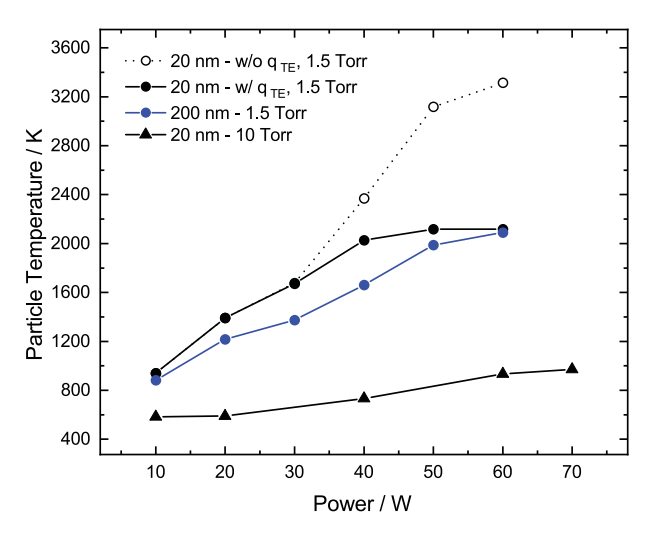


Figure 10. Steady-state mean temperatures of Cu₅₂Zr₄₈ particles inside the intense zone.

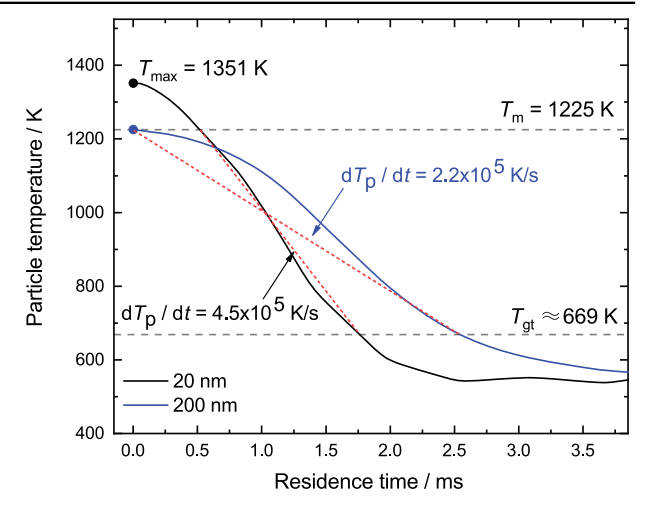


Figure 11. Quenching of 20 and 200 nm $Cu_{45}Zr_{55}$ particles at 20 W and at 1.5 Torr as they leave the intense zone.

200 nm particle within range of plasma parameters investigated, as the mean temperatures calculated by accounting for thermionic emission turned out to be very close to the values calculated when thermionic emission was neglected. The reason stems from the fact that the Schottky effect is size dependent, and the electric field on a smaller charged particle is usually higher. Furthermore, increasing the pressure is accompanied by increased Knudsen cooling rates and decreased ion density (figure 4). Therefore, particle temperatures were much lower at 10 Torr, and the maximum mean temperature of a 20 nm particle stayed below 1000 K.

The quenching rate of particles is sufficiently fast to arrest an amorphous state from the liquid melt that is expected to form in the intense zone. The residence time in the intense zone is very short, approximately 1 ms due to high flow velocities, which range from 6 to $10 \,\mathrm{m\,s^{-1}}$ at 1.5 Torr depending on axial position. The temperatures of 20 and 200 nm CuZr nanoparticles as a function of time, after the peak temperature has been reached, are plotted in figure 11. The nanoparticles cool from the melting point to the glass transition temperature $T_{\rm gt}$ at a rate greater than $10^5\,{\rm K\,s^{-1}}$, which is sufficiently fast to arrest the amorphous state for CuZr [32]. At positions further downstream, the temperature of the particles stay below $T_{\rm gt}$ (see figure 9(a)). Therefore, it appears feasible to transform crystalline CuZr NPs into an amorphous state using the ion density profile naturally present in the archetypal flow-through RF plasma reactor. Based on the results given in figure 10, melting larger particles would be feasible at higher powers. However, external cooling may be required to maintain the reactor temperature below the crystallization temperature of the metal.

Although the example presented herein was for CuZr alloy, other marginal metallic glasses could probably also be synthesized due to the similar requisite quenching rates, e.g. PdSi [55] or NiZr [56]. The possibility of forming amorphous particles should primarily depend on the maximum particle temperatures reached in the intense zone, which would dictate whether particles would melt or not. Therefore, the melting

temperature is a threshold temperature of the process that needs to be surpassed. This threshold temperature is reminiscent of plasma synthesis of crystalline silicon particles, where crystallinity requires particles to reach temperatures above the crystallization temperature [57]. In order to reach the threshold particle temperature in the LTP, ion densities should be high enough. As shown by the particle temperature histories and maximum steady-state temperatures in figures 9 and 10, however, the maximum temperature achieved in the LTP also depends on the ion density distribution, gas temperature, particle residence time and particle thermal inertia. For particles that melt in the intense zone, forming an amorphous phase is then primarily determined by the background gas temperature and by the ion densities in the lowintensity plasma downstream of the powered electrode. If the reactor can be tuned in such a way that the background gas temperature is kept sufficiently low while the ion density can be increased predominantly at the intense zone, then theory suggests that the quenching rates could be increased to orders even higher than $10^5 \,\mathrm{K \, s^{-1}}$. As presented in figure 9, larger particles are more difficult to heat up due to their higher heat capacity. On the other hand, particles smaller than 10 nm are also expected to be difficult to make amorphous. In the case of smaller nanoparticles, the nonequilibrium acts against the formation of an amorphous phase since the charging is stochastic and the low heat capacities of particles allow heat spikes to occur. Heat spikes continuously elevate nanoparticle temperature and then the particle gets quenched. Since heat spikes, which are of magnitude large enough to elevate very small nanoparticles above the glass transition temperature, can occur in a large region of the plasma, i.e. outside the intense zone; re-crystallization is expected to be pronounced, and the formation of an amorphous phase might therefore be difficult.

The process discussed in this paper can be experimentally accomplished with a configuration that is similar to the one described in [19]. An aerosol generator can be used to generate the CuZr aerosol with particles of the sizes considered in the calculations. As nanopowder of CuZr is commercially available, a dust dispenser would be capable of providing a constant feed of the aerosol into the LTP.

Conclusion

It was shown that the unique nonequilibrium environment of tubular flow-through LTP reactors should theoretically be capable of converting crystalline particles into amorphous particles in-flight, by rapid heating, melting, and subsequent quenching. According to the model calculations, high ion densities in the zone surrounded by the powered electrode can heat particles above 2000 K at moderate input powers. Such temperatures are high enough to melt an extensive list of metals and alloys. The range of applicability for the process described herein depends on the extent of decoupling of the ion density in the intense zone from the ion density down-stream. Furthermore, gas temperatures should be kept

sufficiently low downstream of the intense zone to prevent recrystallization.

Acknowledgments

This work is supported by the National Science Foundation under grant agreement PHY-1702334. The authors would like to thank to Bird Technologies for the use of a VIP power measurement device to measure the energy efficiency of the matching network.

ORCID iDs

E Thimsen https://orcid.org/0000-0002-7619-0926

References

- Mangolini L and Kortshagen U 2007 Plasma-assisted synthesis of silicon nanocrystal inks Adv. Mater. 19 2513–9
- [2] Gresback R, Holman Z and Kortshagen U 2007 Nonthermal plasma synthesis of size-controlled, monodisperse, freestanding germanium nanocrystals *Appl. Phys. Lett.* 91 093119
- [3] Pi X D and Kortshagen U 2009 Nonthermal plasma synthesized freestanding silicon–germanium alloy nanocrystals *Nanotechnology* 20 295602
- [4] Gresback R, Hue R, Gladfelter W L and Kortshagen U R 2011 Combined plasma gas-phase synthesis and colloidal processing of InP/ZnS core/shell nanocrystals *Nanoscale Res. Lett.* 6 68
- [5] Felbier P, Yang J, Theis J, Liptak R W, Wagner A, Lorke A, Bacher G and Kortshagen U 2014 Highly luminescent zno quantum dots made in a nonthermal plasma Adv. Funct. Mater. 24 1988–93
- [6] Thimsen E, Kortshagen U R and Aydil E S 2015 Nonthermal plasma synthesis of metal sulfide nanocrystals from metalorganic vapor and elemental sulfur J. Phys. Appl. Phys. 48 314004
- [7] Lin P A and Sankaran R M 2011 Plasma-assisted dissociation of organometallic vapors for continuous, gas-phase preparation of multimetallic nanoparticles *Angew. Chem.*, *Int. Ed.* 50 10953–6
- [8] Woodard A, Xu L, Barragan A A, Nava G, Wong B M and Mangolini L 2017 On the non-thermal plasma synthesis of nickel nanoparticles *Plasma Process. Polym.* 15 1700104
- [9] Kortshagen U R, Sankaran R M, Pereira R N, Girshick S L, Wu J J and Aydil E S 2016 Nonthermal plasma synthesis of nanocrystals: fundamental principles, materials, and applications *Chem. Rev.* 116 11061–127
- [10] Daugherty J E and Graves D B 1993 Particulate temperature in radio frequency glow discharges J. Vac. Sci. Technol. A 11 1126–31
- [11] Swinkels G H P M, Kersten H, Deutsch H and Kroesen G M W 2000 Microcalorimetry of dust particles in a radio-frequency plasma J. Appl. Phys. 88 1747–55
- [12] Maurer H, Basner R and Kersten H 2008 Measuring the temperature of microparticles in plasmas *Rev. Sci. Instrum.* 79 093508
- [13] Lampe M, Gavrishchaka V, Ganguli G and Joyce G 2003 Trapped ion effect on shielding, current flow, and charging of a small object in a plasma *Phys. Plasmas* 10 1500–13

- [14] Khrapak S A et al 2005 Particle charge in the bulk of gas discharges Phys. Rev. E 72 016406
- [15] Khrapak S A and Morfill G E 2006 Grain surface temperature in noble gas discharges: refined analytical model *Phys*. *Plasmas* 13 104506
- [16] Mangolini L and Kortshagen U 2009 Selective nanoparticle heating: another form of nonequilibrium in dusty plasmas *Phys. Rev.* E 79 026405
- [17] Kramer N J, Anthony R J, Mamunuru M, Aydil E S and Kortshagen U R 2014 Plasma-induced crystallization of silicon nanoparticles J. Phys. Appl. Phys. 47 075202
- [18] Lopez T and Mangolini L 2016 In situ monitoring of hydrogen desorption from silicon nanoparticles dispersed in a nonthermal plasma J. Vac. Sci. Technol. B 34 041206
- [19] Uner N B and Thimsen E 2017 In-flight size focusing of aerosols by a low temperature plasma J. Phys. Chem. C 121 12936–44
- [20] Woodard A, Shojaei K, Nava G and Mangolini L 2018 Graphitization of carbon particles in a non-thermal plasma reactor *Plasma Chem. Plasma Process.* 38 683–94
- [21] Turnbull D 1981 Metastable structures in metallurgy Metall. Trans. B 12 217–30
- [22] Zhou S, Pi X, Ni Z, Luan Q, Jiang Y, Jin C, Nozaki T and Yang D 2014 Boron-and phosphorus-hyperdoped silicon nanocrystals Part. Part. Syst. Charact. 32 213–21
- [23] Cahn R W and Haasen P 1996 *Physical Metallurgy* vol 2 (North-Holland: Amsterdam)
- [24] Luborsky F E 1983 Amorphous Metallic Alloys (London: Butterworths)
- [25] Wongpiya R, Ouyang J, Chung C-J, Duong D T, Deal M, Nishi Y and Clemens B 2015 Structural and electrical characterization of CoTiN metal gates *J. Appl. Phys.* 117 075304
- [26] Ouyang J, Wongpiya R, Deal M D, Clemens B M and Nishi Y 2015 Amorphorized tantalum–nickel binary films for metal gate applications Appl. Phys. Lett. 106 151903
- [27] Molnáar Å, Smith G V and Bartók M 1989 New catalytic materials from amorphous metal alloys *Advances in Catalysis* ed D D Eley *et al* vol 36 (New York: Academic) pp 329–83
- [28] Mangolini L, Thimsen E and Kortshagen U 2005 High-yield plasma synthesis of luminescent silicon nanocrystals *Nano Lett.* 5 655–9
- [29] Altounian Z, Guo-hua T and Strom-Olsen J O 1982 Crystallization characteristics of Cu–Zr metallic glasses from Cu₇₀Zr₃₀ to Cu₂₅Zr₇₅ J. Appl. Phys. 53 4755–60
- [30] Gasser D and Baiker A 1989 Hydrogenation of carbon dioxide over copper–zirconia catalysts prepared by in situ activation of amorphous copper–zirconium alloy Appl. Catal. 48 279–94
- [31] Martinek T, Molnár Á, Katona T, Bartók M and Lovas A 1996 Amorphous alloy catalysis IX. Isomerization and hydrogenation of allyl alcohol over an amorphous copper– zirconium alloy J. Mol. Catal. Chem. 112 85–92
- [32] Gillessen F and Herlach D M 1988 Crystal nucleation and glass-forming ability of Cu–Zr in a containerless state *Mater. Sci. Eng.* 97 147–51
- [33] Johnson E O and Malter L 1950 A floating double probe method for measurements in gas discharges *Phys. Rev.* 80 58–68
- [34] Borodai S P and Betina T A 1988 Temperature dependence of the emissivity of nonporous quartz ceramic *J. Appl. Spectrosc.* 48 92–7
- [35] Roth C, Bornholdt S, Zuber V, Sonnenfeld A, Kersten H and von Rohr P R 2011 Comparison of calorimetric plasma

- diagnostics in a plasma downstream reactor *J. Phys. Appl. Phys.* 44 095201
- [36] Kennedy J L and Djeu N 2002 Operation of Yb:YAG fiberoptic temperature sensor up to 1600 °C Sensors Actuators Phys. 100 187–91
- [37] Kennedy J L and Djeu N 2003 Energy transfer in rare earth doped Y₃Al₅O₁₂ at very high temperatures *J. Lumin.* 101 147–53
- [38] Raizer Y 1997 Gas Discharge Physics (Berlin: Springer)
- [39] Fortov V, Ivlev A, Khrapak S, Khrapak A and Morfill G 2005 Complex (dusty) plasmas: current status, open issues, perspectives *Phys. Rep.* 421 1–103
- [40] Shah R K and London A L 1978 Laminar Flow Forced Convection in Ducts: A Source Book for Compact Heat Exchanger Analytical Data (New York: Academic)
- [41] Matsoukas T and Russell M 1995 Particle charging in lowpressure plasmas *J. Appl. Phys.* 77 4285–92
- [42] Khrapak S A and Morfill G E 2008 An interpolation formula for the ion flux to a small particle in collisional plasmas *Phys. Plasmas* 15 114503
- [43] Sherman F S 1962 A survey of experimental results and methods for the transition regime of rarefied gas dynamics Rarefied Gas Dynamics—Proc. 3rd Int. Symp. on Rarefied Gas Dynamics vol 2 (Paris, 1962) ed J A Laurmann pp 245–9
- [44] Piejak R, Godyak V, Alexandrovich B and Tishchenko N 1998 Surface temperature and thermal balance of probes immersed in high density plasma *Plasma Sources Sci. Technol.* 7 590–8
- [45] Friedlander S K 2000 Smoke, Dust, and Haze: Fundamentals of Aerosol Dynamics (New York: Oxford University Press)
- [46] Knudsen M 1950 *The Kinetic Theory of Gases: Some Modern Aspects* (London: Methuen)
- [47] Bohren C F and Huffman D R 2004 Absorption and Scattering of Light by Small Particles (Weinheim: Wiley-VCH)
- [48] Selamet A and Arpaci V S 1989 Rayleigh limit—Penndorf extension *Int. J. Heat Mass Transfer* 32 1809–20
- [49] Vanfleet R R and Mochel J M 1995 Thermodynamics of melting and freezing in small particles Surf. Sci. 341 40–50
- [50] Clements R M 1978 Plasma diagnostics with electric probes J. Vac. Sci. Technol. 15 193–8
- [51] Thimsen E 2018 Beyond equilibrium thermodynamics in the low temperature plasma processor *J. Vacuum Sci. Technol.* B 36 048501
- [52] Lopez T and Mangolini L 2014 On the nucleation and crystallization of nanoparticles in continuous-flow nonthermal plasma reactors J. Vac. Sci. Technol. B 32 061802
- [53] Le Picard R, Markosyan A H, Porter D H, Girshick S L and Kushner M J 2016 Synthesis of silicon nanoparticles in nonthermal capacitively-coupled flowing plasmas: processes and transport *Plasma Chem. Plasma Process.* 36 941–72
- [54] Askari S, Levchenko I, Ostrikov K, Maguire P and Mariotti D 2014 Crystalline Si nanoparticles below crystallization threshold: effects of collisional heating in non-thermal atmospheric-pressure microplasmas Appl. Phys. Lett. 104 163103
- [55] Masumoto T and Maddin R 1971 The mechanical properties of palladium 20 a/o silicon alloy quenched from the liquid state Acta Metall. 19 725–41
- [56] Jiang H G and Baram J 1996 Estimation of the glass transition temperature in metallic glasses *Mater. Sci. Eng.* A 208 232–8
- [57] Kramer N J, Aydil E S and Kortshagen U R 2015 Requirements for plasma synthesis of nanocrystals at atmospheric pressures J. Phys. Appl. Phys. 48 035205